



## Frequent estuarine engineering exacerbates flood risk in the Greater Bay Area

Ping Zhang , Haichen Liu , Huayang Cai , Suying Ou , Zhijun Dai , Jianliang Lin & Qingshu Yang

To cite this article: Ping Zhang , Haichen Liu , Huayang Cai , Suying Ou , Zhijun Dai , Jianliang Lin & Qingshu Yang (2025) Frequent estuarine engineering exacerbates flood risk in the Greater Bay Area, Engineering Applications of Computational Fluid Mechanics, 19:1, 2528535, DOI: [10.1080/19942060.2025.2528535](https://doi.org/10.1080/19942060.2025.2528535)

To link to this article: <https://doi.org/10.1080/19942060.2025.2528535>



© 2025 The Author(s). Published by Informa UK Limited, trading as Taylor & Francis Group.



View supplementary material [↗](#)



Published online: 09 Jul 2025.



Submit your article to this journal [↗](#)



View related articles [↗](#)



View Crossmark data [↗](#)

# Frequent estuarine engineering exacerbates flood risk in the Greater Bay Area

Ping Zhang<sup>a</sup>, Haichen Liu<sup>b</sup>, Huayang Cai<sup>b</sup>, Suying Ou<sup>b</sup>, Zhijun Dai<sup>a</sup>, Jianliang Lin<sup>b</sup> and Qingshu Yang<sup>b</sup>

<sup>a</sup>State Key Laboratory of Estuarine and Coastal Research, East China Normal University, Shanghai, People's Republic of China; <sup>b</sup>School of Ocean Engineering and Technology, Sun Yat-Sen University, Zhuhai, People's Republic of China

## ABSTRACT

Global mega-bay systems are experiencing intensive estuarine engineering (e.g. dredging and reclamation), yet the compound effects and underlying mechanisms driving flood risk amplification remain insufficiently quantified. This study investigates flood risk changes in the Bay-Inlet-Channel system of China's Greater Bay Area (ranked as the world's fourth largest mega-bay) through extreme value analysis of 1965–2017 water level records using generalized extreme value (GEV) theory and max-stable process modelling. Our results demonstrate spatially heterogeneity in flood risk trends, with differential extreme water level rise changes: 0.22 cm/yr at the bay mouth, 0.65 cm/yr in the inner bay, and 0.56 cm/yr in the upper tidal reach (Shiziyang), coinciding with a risk escalation from Category II (strong) to Category I (extreme). Hydrodynamic analysis reveals that deposition-induced tidal range attenuation at the bay mouth partially moderates flood risk acceleration, whereas synergistic effects of erosional dredging and convergent reclamation amplify both tidal and surge dynamics, consequently exacerbating flood risk in the inner bay, with the tidal reach exhibiting intermediate trends due to energy dissipation through Humen Inlet. Numerical simulations quantify maximum impacts on extreme high water levels, with 9.61% rising associated with slower-propagating waves from reclamation and 3.33% decreased with faster-propagating waves induced by dredging. Projections under SSP5-8.5 sea-level rise scenarios indicate that extreme high water levels will surpass optimized 300-yr return levels defense standards by 2080 (outer bay), 2090 (inner bay), and 2100 (tidal reach). These findings provide critical insights into global flood risk management in engineered mega-bay systems and advance methodological frameworks for extreme water level assessment.

## ARTICLE HISTORY

Received 16 May 2025  
Accepted 28 June 2025




## KEYWORDS

Estuarine engineering; flood risk; dredging and reclamation; greater bay area; tide-dominant estuary

## 1. Introduction

Estuaries, characterized by low-lying terrain and high population density, exhibit acute vulnerability to coastal flooding, a global hazard responsible for hundreds of thousands of deaths and billions in infrastructure damage annually (Edmonds et al., 2020; Haigh et al., 2016; Rentschler et al., 2023). Notably, current estimates indicate approximately 334 million inhabitants occupy 85% of global estuaries (Chan et al., 2024), where rapid urbanization has emerged as the predominant factor exacerbating human exposure and vulnerability to flood risk (Rentschler et al., 2022). Flood mechanisms can be categorized into three primary categories according to their formation process: (1) rainfall-induced floods caused by extreme precipitation (Nanditha & Mishra, 2025); (2) riverine floods resulting from upstream overflow (Munoz et al., 2018); and (3) coastal floods triggered by astronomical tides, storm surges, and strong winds

(Hu et al., 2023; Ma et al., 2022; You et al., 2024). Among these, storm tide-driven coastal flooding typically causes the most severe damage (Tadesse et al., 2022). Global observational records since 1990 reveals a significant increase in flooding damages caused by tropical cyclone, especially in the mega-bay systems like New York Bay and San Francisco Bay in US and Tokyo Bay in Japan (Hoshino et al., 2016; Lowe et al., 2024; Russo et al., 2013; Talke et al., 2014). The Greater Bay Area (GBA) of China, recognized as the world's fourth major mega-bay encompassing the Pearl River Delta (PRD) region with a population exceeding 70 million (Wang & Rainbow, 2020), has shown particular vulnerability to coastal flooding. In recent decades, Guangdong Province showing particular vulnerability, recording the highest frequency of such events and corresponding economic losses within the Greater Bay Area (Wang et al., 2021), assessing and explaining its long-term changes of storm

**CONTACT** Zhijun Dai  zjdai@sklec.ecnu.edu.cn  State Key Laboratory of Estuarine and Coastal Research, East China Normal University, Shanghai 200241, People's Republic of China; Jianliang Lin  linjliang7@mail.sysu.edu.cn School of Ocean Engineering and Technology, Sun Yat-Sen University, Zhuhai 519082, People's Republic of China

 Supplemental data for this article can be accessed online at <https://doi.org/10.1080/19942060.2025.2528535>.

© 2025 The Author(s). Published by Informa UK Limited, trading as Taylor & Francis Group.  
This is an Open Access article distributed under the terms of the Creative Commons Attribution License (<http://creativecommons.org/licenses/by/4.0/>), which permits unrestricted use, distribution, and reproduction in any medium, provided the original work is properly cited. The terms on which this article has been published allow the posting of the Accepted Manuscript in a repository by the author(s) or with their consent.

tide-driven coastal flooding is vitally significant and urgent.

Extensive research has characterized tropical cyclone impacts through both observational data and numerical modelling, with particularly focus on wind velocity, surge level, and their interactions with astronomical tides and river discharge (Doodson, 1956; Hu et al., 2007, 2023; Stephens et al., 2020; Zhuge et al., 2024). These studies have elucidated the complex hydrodynamics interactions between storm surges, tidal forces, river discharge (Arns et al., 2020; Palmer et al., 2019; Rego & Li, 2010). In addition, climate change, inducing sea-level rise with a speed of  $2.9 \pm 0.2$  mm/yr, has been shown to exacerbate flooding through enhanced nonlinearities (Idier et al., 2019; Yang et al., 2021), with stronger impacts during peak tide periods (Ma et al., 2022). Coastal urbanization and population growth were identified as major contributing factors (Klotzbach et al., 2025; Meiler et al., 2022), while the frequent anthropogenic interventions, including channel dredging, land reclamation, sand mining, and bridge construction, have substantially benefited socioeconomic development (Hoitink et al., 2020), their cumulative effects on morphological alterations and subsequent flood risk amplification require more rigorous quantification.

Estuarine engineering intervention, particularly channel dredging and land reclamation, emerge as dominant anthropogenic factors altering estuarine bathymetric like depth, width, and convergence, subsequently modifying the inertia-friction-convergence balance, and ultimately amplifying tidal ranges (Guo et al., 2022; Schrijvershof et al., 2024; Van Maren et al., 2023). Additionally, tidal flat loss from reclamation increases wave energy and storm vulnerability (De Dominicis et al., 2023; Mondal et al., 2024; Zhang et al., 2021a). Global urban areas are experiencing escalating flood risk (Vousdoukas et al., 2018), evidenced by rising storm surge trends of 3 mm/yr in Hong Kong (You et al., 2024), 1.5 mm/yr in New York (Wahl et al., 2015), and a 26% increase in 25-year flood exceedance depth in the San Francisco Bay Area (Russo et al., 2013). However, critical knowledge gaps remain regarding how sustained morphological alterations from dredging and reclamation affect long-term flooding patterns.

Globally, funnel-shaped, tide-dominant channels exhibit consistent patterns of anthropogenic tidal amplification (Dai et al., 2016; Hoitink et al., 2020; Wang et al., 2015). The Greater Bay Area (GBA), encompassing the majority of the Pearl River Delta (PRD) region with a total population exceeding 70 million (Wang & Rainbow, 2020), contains a system comprising interconnected Lingding Bay, Humen Inlet, and Shiziyang Tidal Channel that forms a complex Bay-Inlet-Channel (BIC)

system, representing the primary hydrodynamics regime of the Guangdong-Hong Kong-Macao Greater Bay Area. Since 1960, Lingding Bay has experienced unprecedented tidal changes, with constituent amplitudes and tidal range increasing anomalously (Zhang et al., 2021b; Chu et al., 2022). These transformations coincide with intensive human interventions, shipping channels in Lingding Bay's Western Channel (Fu et al., 2025; Wu et al., 2016), Humen Inlet deep channel (Wu et al., 2010, 2006) and Shiziyang have deepened double through frequent dredging and sand mining. Combined with its documented vulnerability to flooding from storm events, the BIC is a typical funnel-shaped location to examine how bathymetric alterations modify both tidal dynamics and storm surge behaviour (Jay, 1991; Savenije et al., 2008). Recent studies confirm that anthropogenic interventions have exacerbated compound flood risk (She et al., 2023; You et al., 2024) within GBA, while the underlying mechanism is still unclear.

Therefore, this study systematically evaluates the exacerbating effects of the typical estuarine engineering (dredging and reclamation) on storm-driven flood risk in the BIC system of Pearl River Estuary within Greater Bay Area. Our investigation proceeds through four sequential analyses: (1) decadal-scale assessment of bathymetric changes induced by dredging and reclamation (1960s–2020s); (2) flood risk evaluation across the Greater Bay Area using daily water level records (1965–2017) and max-stable modelling approaches; (3) identification and quantification of dominant flood drivers, particularly the relative contributions of channel dredging versus land reclamation; and (4) development of a future risk assessment framework aligned with GBA flood protection standards, accompanied by adaptive management strategies.

## 2. Materials and methodology

### 2.1. Features of the complex system

The Pearl River Estuary (PRE, Figure 1b) represents one of the world's most complex channel network systems, draining an area of 450,000 km<sup>2</sup>. This highly urbanized and industrialized region (Zhou et al., 2018) is characterized by extensive freshwater discharge through a dense tributary network with relatively low suspended sediment concentrations. The system receives water primarily from three major tributaries (West, North, and East Rivers) and discharges into the South China Sea through eight major outlets (Yamen, Hutiaomen, Jiti-men, Modaomen, Hengmen, Hongqimen, Jiaomen, and Humen). As China's second largest river system, the Pearl River delivers approximately 282.3 billion m<sup>3</sup> of

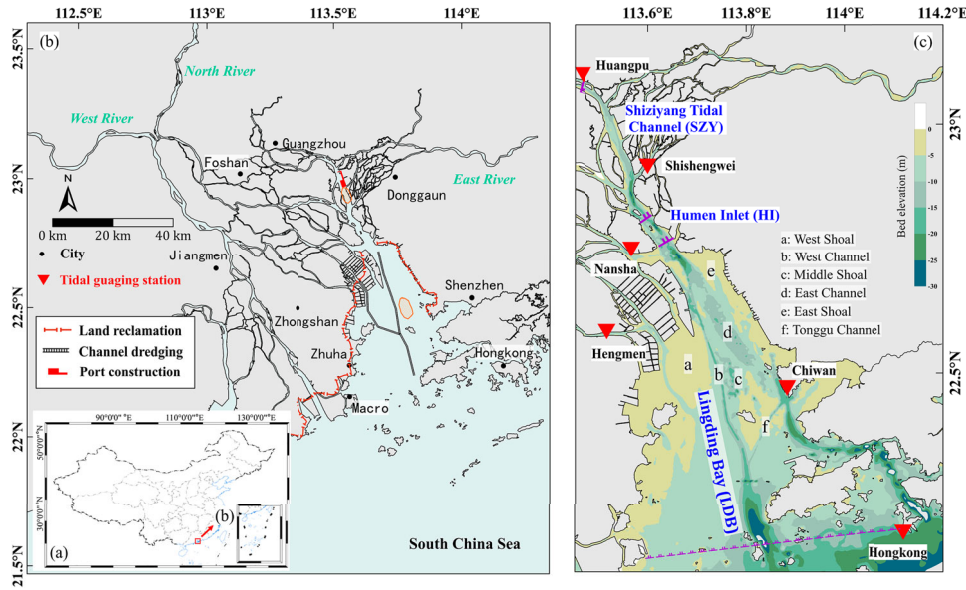


**Figure 1.** Overview of the Pearl River Delta (a) and the Bay-Inlet-Channel (BIC) system showing the locations of six hydrological monitoring stations (b).

freshwater and 72 million tons of sediment annually (Liu et al., 2014), with the West River alone contributing about 215 billion  $\text{m}^3/\text{yr}$  of discharge and 35 million  $\text{kg/s}$  of sediment flux (Zhang et al., 2013). In addition, the Pearl River Delta exhibits a mean annual discharge of 8,952  $\text{m}^3/\text{s}$  and experiences a mixed semidiurnal tidal regime, with tidal ranges averaging 1.0–1.7 m near the estuary mouths (Zhang et al., 2013).

This research examines the Bay-Inlet-Channel (BIC) system (Figure 1c), a 118 km composite of Lingding Bay (LDB), Humen Inlet (HI), and Shiziyang (SZY) tidal channel, representing a characteristic ‘network-bay’ structure in the Pearl River Estuary’s core area. This system serves critical natural functions (flood discharge, drainage, and tidal exchange) while supporting the Guangdong-Hong Kong-Macao Greater Bay Area’s socioeconomic development. Lingding Bay (LDB), the largest bell-shaped estuary in the PRE, spans 80 km and features a distinct bathymetric configuration comprising three shoals (West, Middle, and East Shoals) and two channels (Western and Eastern Channels). As a tide-dominated system, LDB primarily receives freshwater from the East River before discharging into the South China Sea. Influenced by Pacific Ocean tides, the LDB exhibits a typical tidal range of 1.0–1.77 m. Humen Inlet (HI), a 10-km tide-dominated channel linking LDB and SZY, discharges 60.3 billion  $\text{m}^3/\text{year}$  (18.5% of PRE’s total) with flood-season flows averaging 228.8 billion  $\text{m}^3$  and sediment loads of 8.41 million  $\text{kg/s}$  (12.0% of PRE’s total) (Wu et al., 2018). As the dominant conduit for eastern PRE tidal dynamics, HI conveys 80.5% of the four eastern outlets’ flood tide volume, the highest among all

eight major inlets, facilitating significant sediments and salt transport from the continental shelf.

The Shiziyang (SZY) tidal reach, approximately 28 km long, located the eastern portion of the PRE (Figure 1c), connecting to LDB through the Humen inlet and features distinct shoal-channel morphology. Its bathymetry includes deep scour channels at both estuarine and fluvial boundaries while maintaining a characteristic ‘three-channel-two-shoal’ configuration in mid-reaches (Zhang et al., 2013, 2018). The channel experiences an irregular semidiurnal tidal regime with average ranges of 1.06–1.69 m, demonstrating strong ebb-dominated tidal asymmetry. Moreover, the SZY channel receives the entire discharge from partial of East River network, along with approximately 60% of the North River’s runoff, ultimately draining southward into the South China Sea. With an average annual discharge of 58.6 billion  $\text{m}^3$  (about 19% of the Pearl River Basin’s total) and sediment load of 88.5 million  $\text{kg/s}$  (10% of the basin’s total), the channel’s shoal areas primarily consist of coarse-grained sediments derived from the East River basins.

## 2.2. Datasets

In this study, daily high and low water level time series (1965–2017) from six gauging stations were collected (Figure 1b), including Hongkong (denoted by HK), Chiwan (denoted by CW), Shishengwei (denoted by SSW), Huangpu (denoted by HP), Hengmen (denoted by HM) and Nansha (denoted by NS), and their locations shown in *Supplementary material*. Here, the water level time series in CW, SSW, HP, HM and NS stations were



**Table 1.** Classification of storm surge intensity and exceedance severity.

Classifications	I (Extreme)	II (Strong)	III (Moderate)	IV (Medium)	V (Weak)
Storm surge intensity	$h > 250$	$200 < h \leq 250$	$150 < h \leq 200$	$100 < h \leq 150$	$50 < h \leq 100$
Exceedance severity	Exceeding red alert by $> 70$ cm	Exceeding red alert ( $\leq 70$ cm)	Reaching orange alert	Reaching yellow alert	–

collected from the hydrological data of the Pearl River Basin, and post-2017 water level time series are unfortunately unavailable due to data security restrictions. The water level time series in Hongkong station were collected from the University of Hawaii Sea Level Center (UHSLC, <https://uhslc.soest.hawaii.edu/>, Caldwell et al., 2015). All water levels were corrected to the Pearl River Datum and interpolated by a trigonometric interpolation method (Zhang et al., 2018) into hourly data for harmonic analysis.

Moreover, 2 groups of morphological data of Lingding Bay in 1964 and 2008, Humen Inlet and Shiziyang in 1955 and 2010 were collected from the Guangzhou Maritime Safety Administration and the China Peoples Liberation Army Navy Command Assurance Department of Navigation. Due to the data limitation, we integrate the maps into 2 periods of the BIC system for the 1960s and 2010s. Subsequently, the digital elevation model (DEM) of BIC was generated and the bathymetric data were converted from the local lowest tidal level to the Pearl River Datum. Projected to UTM – WGS84 coordinates of China, the data were interpolated to a  $20 \text{ m} \times 20 \text{ m}$  grid DEM in the ArcGIS software.

To investigate the spatiotemporal distribution features of extreme storm water levels risk in the BIC system, we collected a dataset of typhoon duration periods and paths in offshore China. The dataset was obtained from Oceanographic Data Center, Chinese Academy of Sciences (CASODC <https://datapid.cn/CSTR:33685.11.IOCAS.20210804.001>).

### 2.3. Definition of extreme water levels

We investigate changes of flood risk by exploring variations in extreme water levels caused by storm events, including extreme measured water level (EMWL), astronomical high tide (AHT), maximum storm surge (MSS), and extreme skewed surge (ESS), in response to intensive channel dredging and large-scale land reclamation projects. The data analysis procedures are as follows. First, the daily high and low water levels were interpolated into hourly data using a trigonometric interpolation method (Zhang et al., 2018). Before identifying effective surges in the PRE, the total water levels were decomposed into observed tide and low-frequency surge components using a Godin low-pass filter. This filter, originally developed by Godin (1972) and commonly referred to as the tide killer filter (Candela et al., 1989; Walters & Heston,

1982), was applied to remove short-term (periods shorter than approximately two days) variations in the sea level series.

Subsequently, the predicted astronomical tide was derived through harmonic analysis. The non-tidal residuals were then computed by subtracting the predicted astronomical tide from the observed tide. Finally, the surge was determined by combining the non-tidal residuals with the low-frequency surge components. In this study, we focused on the maximum storm surge (MSS) during each storm event, and its corresponding nearest astronomical high tide (AHT) and extreme measured water level (EMWL), which was shown in *Supplementary material*. Moreover, the extreme skewed surge (ESS) is the level difference between extreme measured water level and the nearest astronomical high tide ( $\text{ESS} = \text{EMWL} - \text{AHT}$ ), representing the non-tidal signal including surge, river discharge, precipitation and their nonlinear interactions (Hague & Talke, 2024; Stephens et al., 2020).

### 2.4. Classification of flood risk

According to national standards (GB/T 39418-2020), the storm surge intensity could be categorized into five levels: Extreme (I), Strong (II), Moderate (III), Medium (IV), Weak (V), with specific classification criteria detailed in Table 1. This intensity classification provides critical information about the physical forcing mechanisms of storm events, which is essential for understanding coastal hydrodynamics and engineering design. Furthermore, tidal gauge stations in the Pearl River Estuary implement a four-tier warning water level system (blue, yellow, orange, and red). By evaluating both the warning level thresholds and the extent to which maximum storm tide levels exceed these benchmarks, the severity of high water level exceedance is classified into four grades: Extreme (I), Strong (II), Moderate (III), Medium (IV), with precise classification parameters provided in Table 1.

To investigate the spatial distribution characteristics of flood risk across the BIC system, we analysed observational data from 1,211 typhoon events captured by six tidal gauge stations during 1965 and 2017. This comprehensive dataset facilitated the classification of both intensity metrics and warning-level exceedance severity for extreme measured water level (EMWL). Here, the storm surge intensity can characterize the meteorological

forcing of Greater Bay Area, while the exceedance severity grading directly relates to coastal flooding impacts and emergency response requirements, offering actionable information for disaster management.

## 2.5. Generalized extreme value (GEV) and max-stable process models

The Generalized Extreme Value (GEV) distribution serves as a cornerstone of extreme value theory, providing a unified framework for modelling the statistical behaviour of extreme events (Lin et al., 2019; Wahl et al., 2017). Its cumulative distribution function (CDF), first introduced by Fisher and Tippett (1928), takes the form:

$$F(x) = \begin{cases} \exp \left\{ - \left[ 1 + \xi \left( \frac{x - \mu}{\sigma} \right) \right]^{-1/\xi} \right\}, & 1 + \xi \left( \frac{x - \mu}{\sigma} \right) > 0 \\ \exp \left\{ - \exp \left( \frac{x - \mu}{\sigma} \right) \right\}, & \xi = 0 \end{cases} \quad (1)$$

where  $\mu$  represents the location parameter,  $\sigma$  is the scale parameter, and  $\xi$  is the shape parameter that determines the tail behaviour of the distribution. Specifically, the GEV distribution encompasses three limiting cases: when  $\xi > 0$ , it corresponds to the heavy-tailed Fréchet distribution; when  $\xi < 0$ , it reduces to the bounded Weibull distribution; and when  $\xi = 0$ , it converges to the light-tailed Gumbel distribution.

To extend the classical univariate Generalized Extreme Value (GEV) distribution to spatial domains, traditional approaches employed hierarchical models (Boumis et al., 2023). However, these methods often fail to adequately capture data-level dependence structures. The max-stable process framework overcomes this limitation by providing a robust approach for modelling multivariate extremes with spatiotemporal dependence (Rashid et al., 2024). Consider  $Y_t(S)$ , where  $t = 1, \dots, T$ , represents years and  $S = s_1, s_2, \dots, s_n$  denotes tide gauge locations in a spatial domain. The process  $Y_t(S)$  is max-stable with GEV marginals if the following limit exists for all locations:

$$Y_t(S) = \lim_{t \rightarrow +\infty} \frac{\max_{i=2}^t Y_t(s) - b_m(s)}{a_m(s)} \quad (2)$$

where  $a_m(s) > 0$  and  $b_m(s)$  are location-specific normalizing constants. The calibration of max-stable processes utilizes pairwise extremal coefficients derived from F-madograms (Stoev, 2010). For any two locations  $s_1$  and

$s_2$ , the F-madogram is computed as:

$$v_F(s_1 - s_2) = \frac{1}{2t} \sum_{i=1}^t |F(z_i(s_1)) - F(z_i(s_2))| \quad (3)$$

where  $z_t(s_1)$  and  $z_t(s_2)$  represent annual maximum surge observations at the respective locations in year  $t$ , and  $T$  is the total observation period. The corresponding extremal coefficient estimate is then obtained through:

$$\hat{\theta}(s_1 - s_2) = \frac{1 + 2v_F(s_1 - s_2)}{1 - 2v_F(s_1 - s_2)} \quad (4)$$

This methodology provides a comprehensive framework for analysing spatial extremes while properly accounting for dependence structures across locations. The max-stable process formulation maintains theoretical consistency with univariate extreme value theory while extending its applicability to spatial contexts. The use of F-madograms for extremal coefficient estimation offers a computationally efficient approach to parameterizing the spatial dependence structure. Finally, the max-stable process was calibrated through an optimization procedure that minimized the sum of squared errors between theoretical and modelled pairwise extremal coefficients.

## 2.6. Validation of extreme water levels

The fitting process was applied to 53 years (1965–2017) of annual maximum (AM) extreme water level from our network of 6 tide gauges distributed around the BIC system. To further evaluate the max-stable model efficiency and estimate the risk of extreme high water level(s) in ungauged locations, we employ a stochastic simulation approach to generate annual maximum extreme water levels along the BIC system by producing 10,000 synthetic annual maximum extreme water level time series at each ungauged location based on the max-stable model's predicted GEV parameters (Rashid et al., 2024). To preserve the observed spatiotemporal variability of annual maximum extreme high water level(s), we implement a rank-ordering technique to match the observed water levels rankings at each tide gauge location. This widely validated method, validated in numerous hydrological applications including synthetic annual maximum extreme water level time series generation, flood forecasting, and ensemble prediction systems (Mehrotra & Sharma, 2019; Scheuerer et al., 2017), effectively maintains the statistical properties of extreme events.

For ungauged locations, we develop a weighted distance-based interpolation scheme that computes surge ranks by averaging observed annual maximum extreme

high water levels ranks by averaging observed annual maximum extreme water level ranks from the two nearest tide gauges, with weights inversely proportional to distance. This approach is physically justified by the characteristic spatial coherence of extreme events (whether tropical cyclones, extra-tropical cyclones, or atmospheric rivers) typically affect extensive coastal stretches, with surge magnitudes decaying gradually with distance from the landfall location (Enriquez et al., 2020; Piecuch et al., 2022). The weighting scheme assumes ungauged locations share similar statistical characteristics (including interannual variability) with proximal tide gauges, consistent with spatial patterns of storm surge events along coastlines.

We employ a leave-one-out cross-validation approach to evaluate the max-stable model's performance in quantifying GEV parameters. This involves iteratively excluding each of the 6 tide gauges, calibrating the model using the Sanzao and Huangjin stations (Table S1 in *Supplementary material*), and predicting the GEV parameters for the omitted tide gauge. Predicted location and scale parameters from this validation were compared against: (1) the parameters obtained from the complete datasets model, and (2) site-specific estimates from univariate GEV distributions. While univariate GEV estimates may not represent absolute truth, they provide a valuable reference for assessing the max-stable model's ability to capture marginal behaviour capture (Cao & Li, 2019).

Model performance was quantified using a relative difference (RD) metric:  $RD = |(Y_{\text{actual}} - Y_{\text{model}})/Y_{\text{actual}}|$ , where  $Y_{\text{actual}}$  and  $Y_{\text{model}}$  represent the reference and model-estimated parameter values, respectively. Both location and scale parameter RDs from leave-one-out validation and univariate GEV distribution in all stations are both less than 0.5, indicating that the model performs reasonably well in predicting GEV parameters (Figure S3 in *Supplementary material*). In addition, the performance of leave-one-out validation is better than univariate GEV distribution. These GEV parameters are subsequently used to calculate extreme surge return period (in years) through the GEV quantile function:  $F^{-1} = (1 - 1/N; \mu, \sigma, \xi)$ , where  $N$  denotes the return period, crucial for designing coastal protection infrastructure. Therefore, by this validation framework, we evaluate the model's performance by comparing simulated and observed extreme high water level (Figure S4 in *Supplementary material*), the mean errors (root mean square errors, RMSE) between observed and median simulated extreme high water level of 8 tidal gauges are less than 0.15 m except from Sanzhao station (Figure S5 in *Supplementary material*).

### 3. Results

#### 3.1. Estuarine engineering effects on morphological evolution

The spatiotemporal patterns of estuarine engineering were investigated, with particular emphasis on channel dredging and land reclamation, and their effects on four representative cross-sections were quantified (Figure 2) through comprehensive analysis of morphological changes in the BIC system (Figure 3). The analysis reveals that reclamation has profoundly narrowed the inner Lingding Bay (LDB), with the western shoreline progressing  $\sim 4.04$  km southeastward (Figure 2a), resulting in an 83.69% maximum width reduction (Figure 3b, d), while eastern shoreline changes remained minimal. This pronounced western constriction has diminished the protective capacity of the west shoal, while enhancing channel convergence and accelerating tidal propagation. Additionally, port construction at XinSha Port resulted in a 0.53 km westward shoreline advancement in the upper SZY (Figure 2a, c), causing a 54.29% channel width reduction (Figure 2b, d) and further amplifying tidal dynamics.

Dredging in the BIC exhibited prolonged, large-scale impacts with intensive excavation depths from 1959 to 2014 (Figure 2b). Phase I (1959: 6.9 m depth) and Phase II (1975–1979: 8.6 m depth) initiated deepening in the inner LDB (Figure 2e) and upper SZY (Figure 2c) by the 1990s. The Guangzhou Port Deepwater Channel Navigation Project (GZ-DCNP), implemented in 1989 (Phase III: 10.5 m depth), deepened the western channels of outer/inner LDB (Figure 2e, f) and established the eastern channel in upper SZY by the 2000s (Figure 2c). Subsequent Phase IV (11.5 m depth) further deepened the western Humen Inlet section (Figure 2d). To accommodate 50,000 deadweight tonnage (DWT) vessels, Phase V (2004 onward: 13.0 m depth) triggered pronounced deepening in outer/inner LDB's western channels (Figure 2e, f), Humen Inlet's eastern side (Figure 2d), and upper SZY's eastern channel (Figure 2c). Concurrently, the Tonggu Navigation Channel's construction necessitated 328.2 million  $\text{m}^3$  of capital dredging. The final Phase VI (achieving 17.0 m depth for 120,000 DWT vessels) implemented between 2014 and 2017 substantially deepened the West Channel and Tonggu Channel in outer LDB by the 2020s (Figure 2f). Subsequently, channel dredging standards have been sustained at 17.0 m, while anthropogenic activities (including channel dredging and sand mining) were prohibited after 2017.

Channel dredging and land reclamation induced rapid accretion with a net souring rate of  $-24.32 \times 10^6 \text{ m}^3/\text{yr}$  from 1960s to 2020s in LDB, comprising a deposition rate

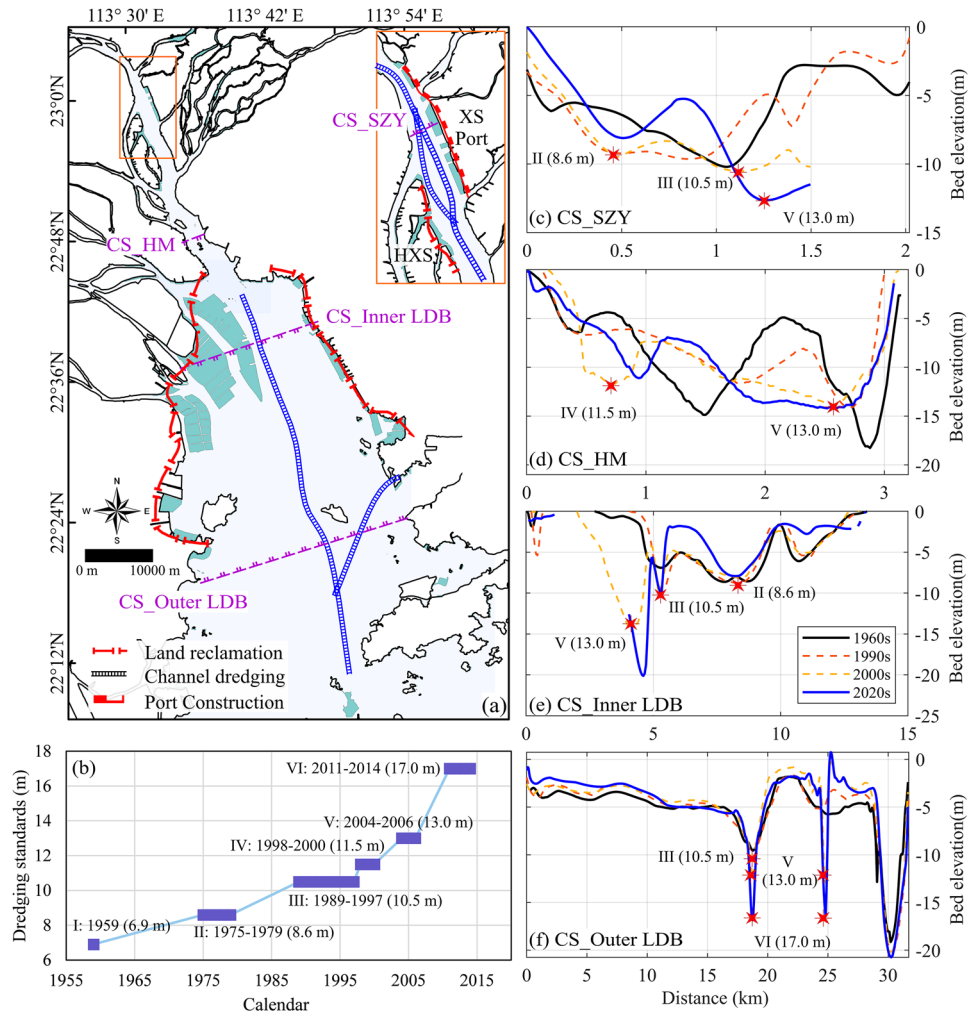


**Figure 2.** Historical anthropogenic modifications (a-b) and consequent bed elevation changes at representative cross-sections (c-f) in the BIC system.

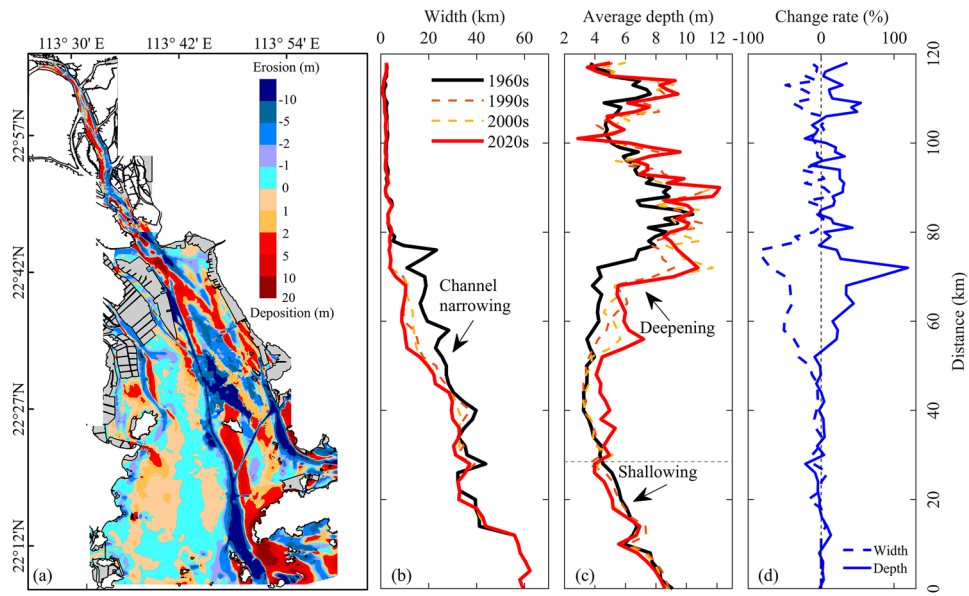


**Figure 3.** Morphodynamic changes in the BIC system: (a) erosion-deposition patterns, (b) channel width variations, and (c) average depth alterations with corresponding change rates (d).



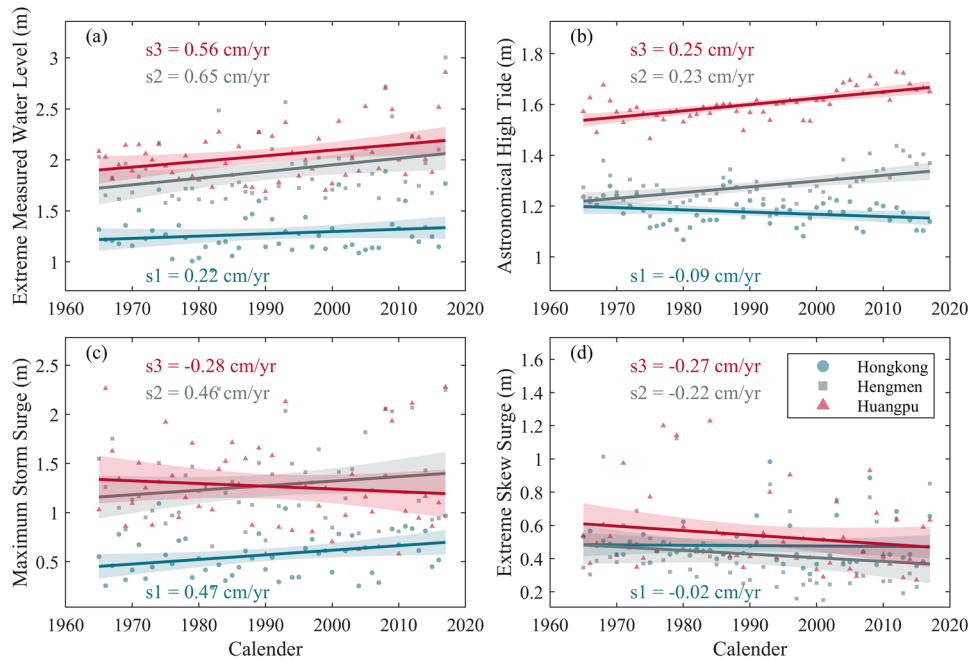


**Figure 4.** Temporal evolution (1965–2017) of annual maximum (a) extreme measured water levels (EMWL), (b) astronomical high tides (AHT), (c) maximum storm surges (MSS), and (d) extreme skew surges (ESS) at three representative stations in the BIC system.

**Table 2.** Erosion and deposition from 1960s to 2020s in different areas of BIC system.

		Lingding Bay	Humen Inlet	Shiziyang
Erosion	Volume ( $10^6 \text{ m}^3/\text{yr}$ )	−65.35	0.35	−1.80
	Area ( $10^6 \text{ m}^2$ )	10.56	7.57	3.13
Deposition	Volume ( $10^6 \text{ m}^3/\text{yr}$ )	41.03	0.56	1.37
	Area ( $10^6 \text{ m}^2$ )	9.36	13.94	2.97
Net	Volume ( $10^6 \text{ m}^3/\text{yr}$ )	−24.32	0.21	−0.43
	Rate (cm/yr)	−1.22	1.00	−0.71

of  $41.03 \times 10^6 \text{ m}^3/\text{yr}$  and an erosion rate of  $-65.35 \times 10^6 \text{ m}^3/\text{yr}$  (Figure 3a and Table 2). This morphodynamic pattern reflects anthropogenically accelerated channel deepening progressing at 1.22 cm/yr. Conversely, the Humen Inlet exhibited net siltation ( $0.21 \times 10^6 \text{ m}^3/\text{yr}$ ), resulting from the balance between  $0.56 \times 10^6 \text{ m}^3/\text{yr}$  deposition and  $-0.35 \times 10^6 \text{ m}^3/\text{yr}$  scouring, demonstrating concurrent severe siltation coupled with intense scouring. Moreover, Figure 3(a) reveals that the SZY manifested net erosion ( $-0.43 \times 10^6 \text{ m}^3/\text{yr}$ ), with  $1.37 \times 10^6 \text{ m}^3/\text{yr}$  deposition and  $-1.80 \times 10^6 \text{ m}^3/\text{yr}$  erosion, exhibiting distinct spatial patterns of eastern erosion versus western deposition.

In addition, the inner LDB (28–80 km) underwent dramatic narrowing (peaking 83.69% reduction near HI at  $y = 76 \text{ km}$ ) and significant deepening (118.93% increase from 4.19 m to 10.75 m at  $y = 72 \text{ km}$ ) between the 1960s–2020s (Figure 3b–d). In contrast, the outer LDB experienced relatively minor width changes but notable shallowing (maximum depth reduction of

21.58%), except for localized deepening in Tonggu Channel (Figure 1c). The constrained Humen Inlet area (80–90 km) maintained relative stability with lower narrowing rates, while still showing 42.87% maximum deepening. Similarly, the SZY displayed substantial morphological changes, with 48.62% maximum narrowing ( $y = 113 \text{ km}$ ) and 54.29% peak deepening. These differential responses reveal a clear spatial segregation, wherein the inner LDB and SZY underwent concurrent narrowing and deepening, in contrast to with the outer LDB's predominant shallowing trend.

### 3.2. Variations of extreme high water levels

To quantify the spatiotemporal evolution of extreme high water level(s) in the Bay-Inlet-Channel (BIC) system within the Greater Bay Area under compound flooding conditions, we analysed the annual maximum (AM) values from 1965 to 2017 at three representative stations: Hongkong (LDB mouth), Hengmen (western LDB), and Huangpu (upper tidal reach in SZY). The analysis demonstrates significant amplification of annual maximum of extreme measured water level (AM-EMWL) (Figure 4a), with upper stations exhibiting 2.5–3 times faster increasing rates ( $s2 = 0.65 \text{ cm/yr}$  and  $s3 = 0.56 \text{ cm/yr}$ ) compared to the mouth ( $s1 = 0.22 \text{ cm/yr}$ ), reflecting combined regional sea-level rise and morphological adjustments. These results reveal an increasing trend in extreme high water level(s) across the Greater Bay Area, with landward-amplified rising rates posing

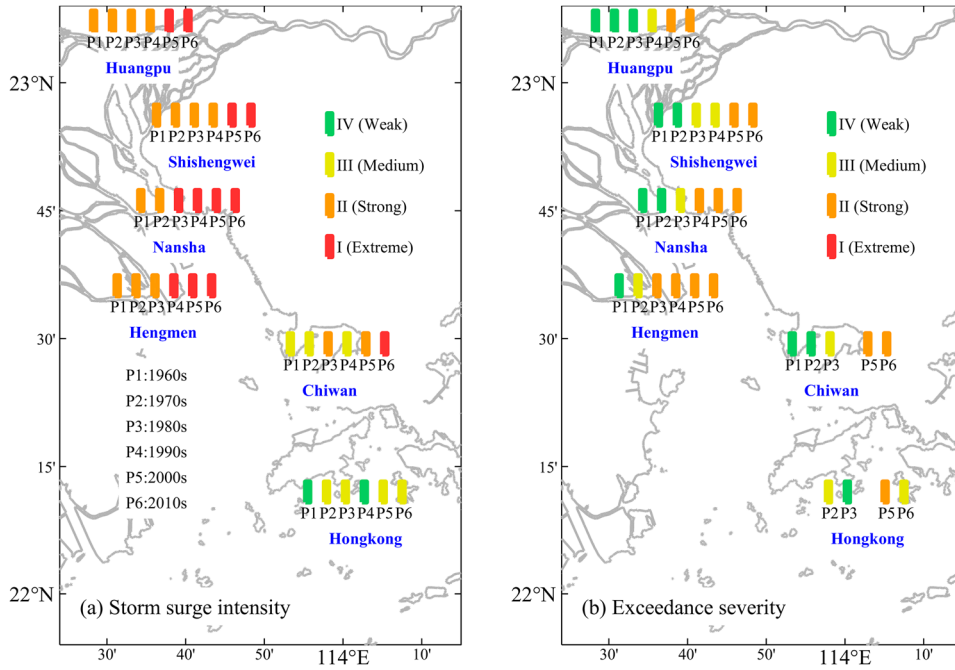


**Figure 5.** Spatiotemporal variations of storm surge intensity (a) and exceedance severity (b)

significant threats to levee safety and increasing flood risk in the upper SZY.

Regarding the flood risk components, the annual maximum of astronomical high tide (AM-AHT) series show contrasting spatial patterns (Figure 4b), with Hongkong station displaying a slight decrease ( $s1 = -0.09$  cm/yr) while both upper stations demonstrate increases ( $s2 = 0.23$  cm/yr,  $s3 = 0.25$  cm/yr), suggesting enhanced tidal dynamics in the inner LDB and SZY regions. The annual maximum of maximum storm surge (AM-MSS) time series exhibit distinct spatial variation (Figure 4c), with comparable increasing rates in LDB ( $s1 = 0.46$  cm/yr,  $s2 = 0.47$  cm/yr) but decreasing trends ( $s3 = -0.28$  cm/yr) in the upper SZY, highlighting fundamentally different surge generation and propagation mechanisms between the convergent bay and tidal channel environments. Notably, annual maximum of extreme skewed surge (AM-ESS) analysis shows system-wide decreasing trends that intensify landward (Figure 4d), with Huangpu's reduction rate ( $-0.27$  cm/yr) being 13.5 times greater than that of Hongkong station ( $-0.02$  cm/yr), implying diminished storm-tide interaction effects, particularly in the inlet-channel (from Humen inlet to SZY) subsystem.

### 3.3. Assessment of flood risk

#### 3.3.1. Spatiotemporal variations of flood risk

Following China's national standard GB/T 39418-2020, we assessed the spatiotemporal variations of flood risk based on annual maximum extreme measured water

levels, revealing lower risk in the outer Lingding Bay (LDB) but elevated risk in the inner LDB and Shiziyang (SZY) regions (Figure 5). The surge intensity in the BIC system exhibited significant intensification from the 1960s to 2010s, as evidenced by the classification upgrades from Medium (IV) to Moderate (III) at Hongkong station, from Moderate (III) to Extreme (I) at Chiwan station, and from Strong (II) to Extreme (I) at inner LDB and SZY stations (Hengmen, Nansha, Shishengwei and Huangpu), with Hongkong station demonstrating this transition earliest in the 1970s and Huangpu station exhibiting the latest in the 2000s (Figure 5a). Regarding exceedance severity, Hongkong station transitioned from no risk in the 1960s to Moderate (III) in the 2010s, while other stations progressed from Medium (IV) to Strong (II) during the same period (Figure 5b). These results indicate significantly increased coastal flood hazards in the BIC system during the 2010s compared to the 1960s under frequent human interventions, particularly in eastern LDB and Deep Bay, where morphological changes caused by land reclamation and channel dredging have most substantially compromised water security in Hong Kong, Shenzhen, and Dongguan cities within the Greater Bay Area.

#### 3.3.2. Estimation of extreme high water return levels

Implementation of the Water Security Plan for the Guangdong-Hong Kong-Macao Greater Bay Area establishes tidal defense capacity benchmarks, mandating Guangzhou and Shenzhen to achieve protection standards exceeding the 200-yr return period (in years) by 2025

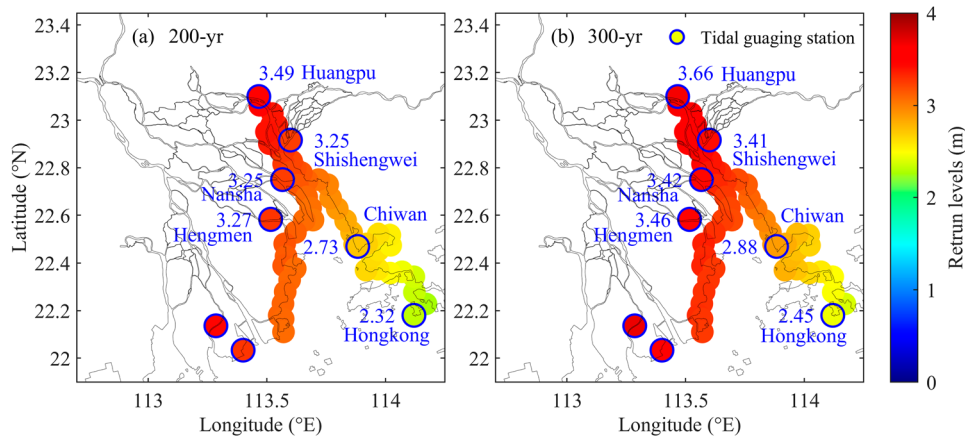


**Figure 6.** Spatial distribution of extreme high water return levels in the BIC system.

(with 100-yr return period requirements for other Pearl River Delta cities), escalating to 300-yr and 200-yr return periods (in years), respectively, by 2035. To evaluate these targets, we estimated the extreme high water return levels (1965–2017) from eight tide gauge stations using a calibrated max-stable process model. Unobserved locations were interpolated via distance-weighted averaging, followed by Monte Carlo simulation (10,000 synthetic annual maximum extreme water level time series) with temporal reshuffling to preserve spatiotemporal variability. This framework generated spatial distributions of extreme high water return levels across the BIC system in the Greater Bay Area (Figure 6).

The assessment of 200-yr and 300-yr return levels demonstrated that the mean values exhibited a progressive increase from 2.87 m in the LDB to 3.26 m in HI and 3.40 m in SZY for the 200-yr return period (Figure 6a), with corresponding values of 3.03, 3.43, and 3.57 m for the 300-yr return period (Figure 6b). Both return periods exhibited a consistent spatial pattern (Figure 6a, b), where western estuarine locations (3.10 m at Hengmen station for 200-yr return periods) consistently yielded higher values than eastern sites (2.64 m at Chiwan station for 200-yr return periods). Of particular significance, the estuary mouth of LDB (2.32 m at Hongkong for 200-yr return period) and upper SZY (3.49 m at Huangpu for 200-yr return period) represented the minimum and maximum observed values, respectively, demonstrating an inland-increasing trend for extreme high-water level and suggesting a higher storm surge risk in the upper reaches of the BIC within the Greater Bay Area.

## 4. Discussions

### 4.1. Driving factors of increasing flood risk

Rising sea levels ( $2.9 \pm 0.2$  mm/yr), driven by climate change, have been shown to amplify flooding risks

through complex nonlinear processes (Idier et al., 2019; Yang et al., 2021). Simultaneously, anthropogenic activities have become a dominant forcing factor in the morphodynamic evolution of estuaries (Hoitink et al., 2020), as evidenced by studies on human-altered in estuarine morphodynamic thresholds of the Yangtze Estuary (Wang et al., 2015; Zhu et al., 2025) century-scale land reclamation effects in Ems Estuary (Schrijvershof et al., 2024). In the Pearl River Estuary (PRE), channel dredging and land reclamation represent the dominant anthropogenic interventions (Cai et al., 2019; Wei et al., 2021). Under the combined forcing of sea-level rise and human-induced morphodynamics and their nonlinear interactions, the BIC system exhibit distinct spatial response patterns on extreme measured water levels (EMWL). Quantitative analysis of long-term variations in astronomical high tide (AHT) and maximum storm surge (MSS), integrated with morphological changes attributable to human activities, reveals the key factors governing these differential responses (Figure 7).

In the outer LDB (represented by Hongkong station), despite channel dredging occurrences in the Tonggu Channel, net deposition prevailed (Figure 3a), resulting in channel narrowing (evidenced by maximum depth decreasing by 21.58% as shown in Figure 3d) and astronomical high tide (AHT) attenuation ( $-0.15$  cm/yr at Hongkong station, presented in Figure 4b). Meanwhile, sea-level rise contributes to increasing maximum storm surge (Calafat et al., 2022), with the maximum storm surge magnitude increasing at a rate of 0.47 cm/yr at Hongkong station (Figure 4c). The opposing trends of astronomical high tide (AHT) and maximum storm surge (MSS), superimposed on rising mean sea level (0.21 cm/yr see Figure S2 in *Supplementary material*), led to a slight increase in extreme measured water level (0.22 cm/yr at Hongkong station, Figure 4a), whereby nonlinear interactions between these components yielded limited compound flooding amplification.

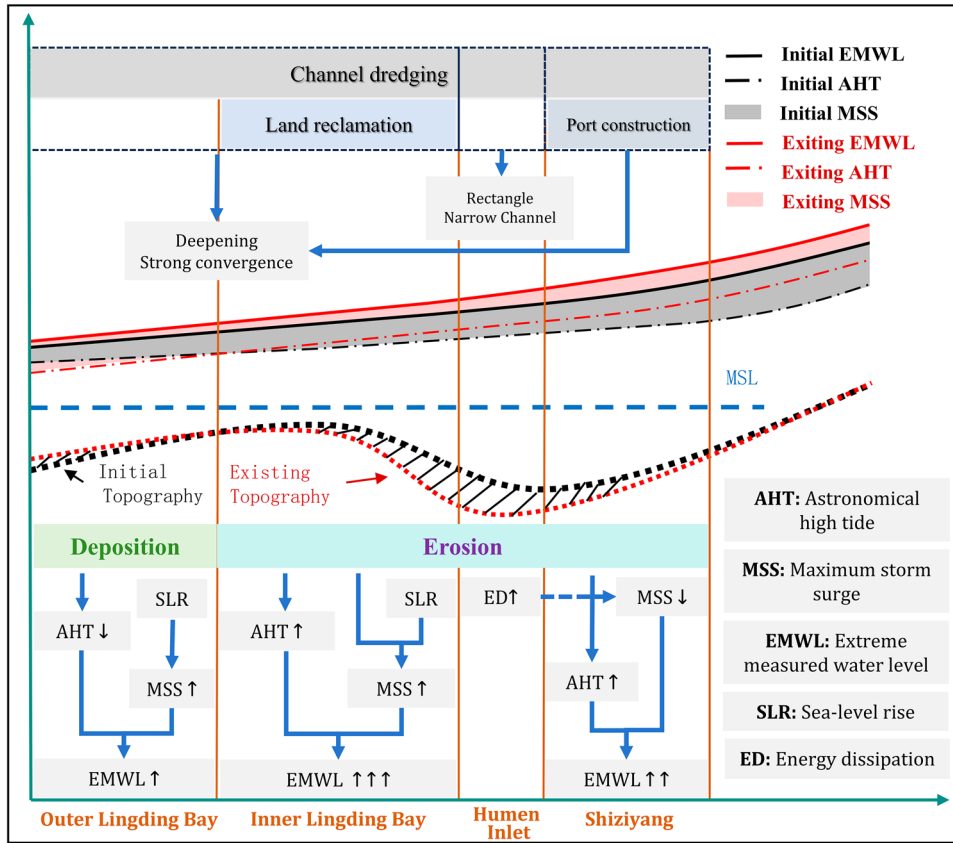


**Figure 7.** Schematic diagram of the mechanisms of flood risk evolution in the BIC system under anthropogenic forcings from channel dredging and land reclamation.

In contrast, the inner LDB experiences more pronounced extreme measured water level increase (0.65 cm/yr at Hengmen station, Figure 4a) due to channel dredging and sand mining that established an erosional regime (Figure 3a) with significant deepening (maximum depth increase of 118.93% shown in Figure 3d), elevating astronomical high tide (0.28 cm/yr at Hengmen station, Figure 4b). Concurrently, reclamation-induced narrowing combined with sea-level rise (0.21 cm/yr, refer to Figure S2 in *Supplementary material*) enhance surge amplification (0.46 cm/yr at Hengmen station, Figure 4c), with the synergistic effects of tidal amplification and surge intensification driving substantial compound flooding escalation.

In the SZY region, the moderate extreme measured water level (EMWL) increase (0.56 cm/yr at Huangpu station, Figure 4a) corresponded to channel deepening (maximum depth increase of 54.29% shown in Figure 3d) that promoted tidal amplification (AHT 0.41 cm/yr) through reduced bottom friction, surpassing the sea level rise of 0.24 cm/yr (Figure S2 in *Supplementary material*). However, enhanced energy dissipation at HI attenuated maximum surges (Wu et al., 2018), manifesting as a decreasing rate of  $-0.19$  cm/yr at Huangpu station, partially counterbalancing the tidal influence and

resulting in an intermediate rate of compound flooding intensification relative to inner LDB.

These results elucidate the differential modulation of extreme measured water level (EMWL) responses across the BIC system by anthropogenic morphodynamic alterations and sea-level rise. Critically, these hydrodynamic responses emerge not merely from the linear superposition of astronomical high tides, extreme storm surges, and sea-level rise components, but rather through their nonlinear synergistic interactions. The spatial heterogeneity in EMWL forcing mechanisms manifests through three distinct regimes: the outer LDB's deposition-dominated regime generated minimal compound flooding changes, while the inner LDB's erosion-surge coupling drove maximum increases, and the SZY's depth-controlled dynamics combined with HI linkage effects yielded intermediate trends. These results provide mechanistic understanding of flood risk evolution under persistent morphological changes.

#### 4.2. Contributions of dredging and reclamation

To further systematically quantify the effects of dredging and reclamation on extreme highwater levels magnitude and propagation characteristics, we employed a validated



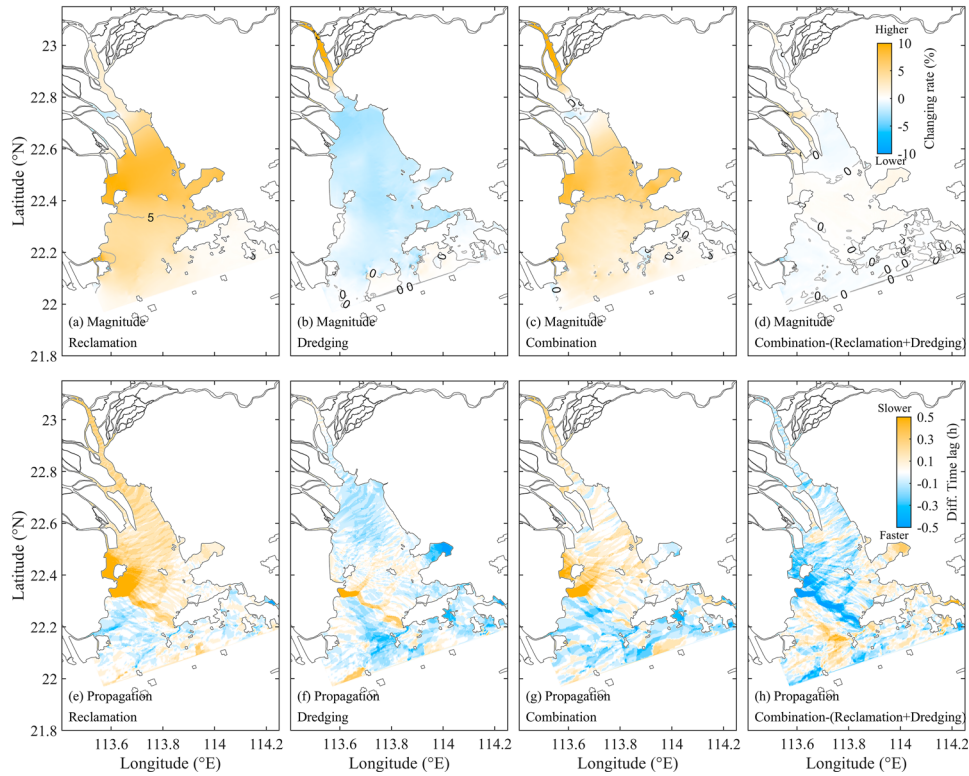


**Figure 8.** Spatiotemporal patterns of (a-d) extreme high-water level magnitudes and (e-h) their propagation dynamics under three anthropogenic scenarios: channel dredging, land reclamation, and their combined effects.

Delft3D-FM numerical model (Figure S6 and Figure S7 in *Supplementary material*) to simulate morphological changes between the 1960s and 2010s under the 2017 Hato storm surge conditions, representing the most severe surge event recorded in the past six decades.

The simulation results reveal that land reclamation intensifies tidal convergence, resulting in elevated extreme high water levels (Figure 8a), with maximum amplification (9.61%) occurring in the inner Lingding Bay and progressively diminishing effects in the upper tidal reach (SZY). However, reclamation activities delay extreme high-water level propagation, as evidenced by increased time lags relative to the Hong Kong reference station, particularly with a 0.5 h delay observed in western Lingding Bay (Figure 8e). Conversely, channel dredging attenuates extreme high-water level in Lingding Bay and Humen Inlet, with a maximum decrease of  $-3.33\%$ , while increasing levels in the Shiziyang tidal reach (Figure 8b). The increased water depth from dredging reduces bottom friction (Famillkhalili & Talke, 2016), thereby accelerating extreme high-water level propagation (Figure 8f). These findings demonstrate opposing flood risk impacts between dredging and reclamation operations.

The synergistic effects of channel deepening and width narrowing exacerbate flood risk through elevated water levels (Figure 8c), with faster propagation

in outer Lingding Bay but slower progression in inner Lingding Bay and Shiziyang (Figure 8g). The combined effect analysis reveals greater extreme high water levels differences in the middle Lingding Bay and upper Shiziyang reach compared to the superposition of individual reclamation and dredging impacts (Figure 8d), along with faster propagation in the BIC system (Figure 8f). This indicates that nonlinear interactions between dredging and reclamation processes lead to synergistic effects that significantly amplify flood risk beyond what would be expected from simple linear addition of individual impacts, demonstrating how concurrent engineering interventions modulate the system's hydrodynamic response through complex interactions between altered channel geometry, tidal dynamics, and energy dissipation patterns.

### 4.3. Optimization of flood risk estimation

Conventional flood risk related to levee security was underestimated due to the limitation of measured water level data and failure to account for spatiotemporal tidal variations from both natural and anthropogenic causes (Zhuge et al., 2024), as evidenced by the 200-yr return level at Nansha station in 2011 (2.86 m) being 0.41 lower than current result (Figure 6a). Conversely, traditional estimation methods frequently overestimated

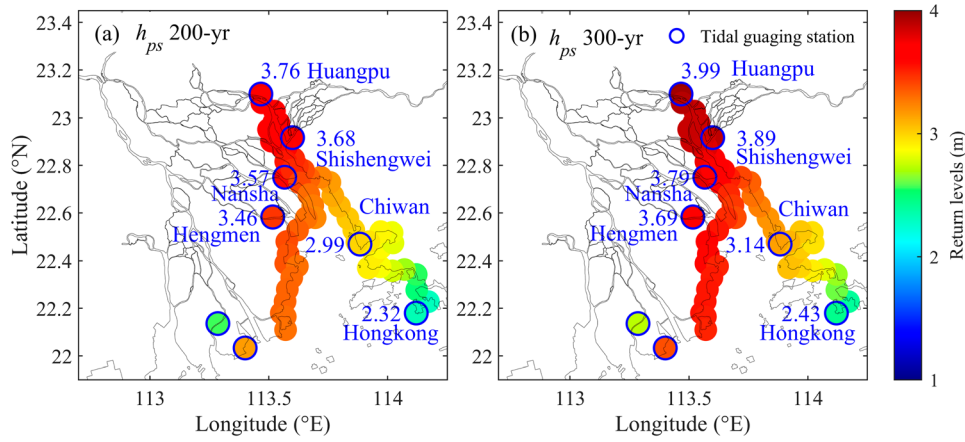


**Figure 9.** Spatial distribution of optimized extreme high water return levels  $h_{ps}$  for (a) 200-yr and (b) 300-yr return periods in the BIC system.

flood risk by up to 30% by neglecting tide-surge interactions (Arns et al., 2020). To overcome this limitation, we developed an improved framework of optimized extreme high water level  $h_{ps} = h_T + h_{(SS, esti)}$  to incorporate spatiotemporal dependence and tide-surge interactions. In this formulation,  $h_T$  represents percentile-based characteristic astronomical tides (5th for declining, 95th for rising trends) derived from annual maximum astronomical high tide analysis of gauging stations (e.g. Figure 7b), while  $h_{(SS, esti)}$  incorporates skew surges estimated via max-stable model (Figure S8 in *Supplementary material*). This approach eliminates biases from direct surge-tide superposition while accounting for morphological changes, thereby avoiding overestimation at locations with declining tides (e.g. Hongkong station) and preventing underestimation where tides are rising (e.g. Huangpu station).

The proposed methodology demonstrates consistent performance across different return periods. For water levels associated with the 200-yr return period, the  $h_{ps}$  averages reached 3.09 m in Lingding Bay, 3.56 m in Humen Inlet, and 3.66 m in Shiziyang, exceeding extreme measured water level by 0.21 m overall (Figure 9a), with the maximal difference at Shishengwei station (+0.43 m). For the 300-yr return period,  $h_{ps}$  values averaged 0.23 m above extreme measured water level, notably at Huangpu station with 3.99 m and exceed 0.33 m (Figure 9b). Validation against Guangzhou Hydrology Bureau and previous study (Pan, 2024) for 200-yr return periods confirmed method reliability (Nansha station  $h_{ps}$ : 3.57 m vs. official 3.39 m and Pan's 3.77 m), demonstrating effective integration of morphodynamic changes for flood risk assessment in the Greater Bay Area. The spatial patterns reveal diminished flood risk in tidal-decline zones (e.g. Hongkong station) versus elevated risks in rising-tide regions.

#### 4.4. Future risks under sea-level rise strategies

Beyond anthropogenic influences, the escalation of extreme water levels associated with sea-level rise (SLR) present significant concerns (Moftakhari et al., 2017; You et al., 2024). This phenomenon accelerates the frequency of currently rare extreme sea levels and differentially modifies storm surge characteristics (Ma et al., 2022; Stephens et al., 2020). We consequently evaluate future extreme high water levels based on projected SLR scenarios from the IPCC Sixth Assessment Report (IPCC, 2023), using maximum observed extreme water levels as baseline (Table S2 in *Supplementary material*).

Figure 10(a,b) demonstrate that by 2150, extreme high water levels may attain 2.57, 2.81, and 3.21 m at the bay mouth (Hong Kong), and 3.32, 3.55, and 3.97 m in inner Lingding Bay (Chiwan) under the three selected IPCC scenarios. The western Lingding Bay exhibits more pronounced increases, projected to reach 3.69, 3.92, and 4.33 m at Hengmen station (Figure 10c). Notably, Shiziyang (Shishengwei, Figure 10e) may experience levels of 3.76, 4.00, and 4.40 m, while the upper tidal reach (Huangpu) could achieve 3.71, 3.92, and 4.36 m by 2150, posing severe flood risk to major metropolitan areas like Guangzhou (Figure 10f).

We additionally project the timeline for extreme high water levels to exceed existing protection standards (optimized 300-yr return levels shown in Figure 9b) across Greater Bay Area stations. Under SSP5-2.6, Chiwan will probably exceed protection thresholds first in 2120, followed by Nansha in 2140. The SSP5-4.5 scenario shows Chiwan exceeding standards by 2090, with Hong Kong and Nansha following suit in 2100, and Hengmen and Shishengwei in 2120 and 2130 respectively. For SSP5-8.5, outer Lingding Bay would exceed thresholds by 2080, inner Lingding Bay by 2090, and the upper tidal reach (SZY) by 2120. These projections suggest that inner

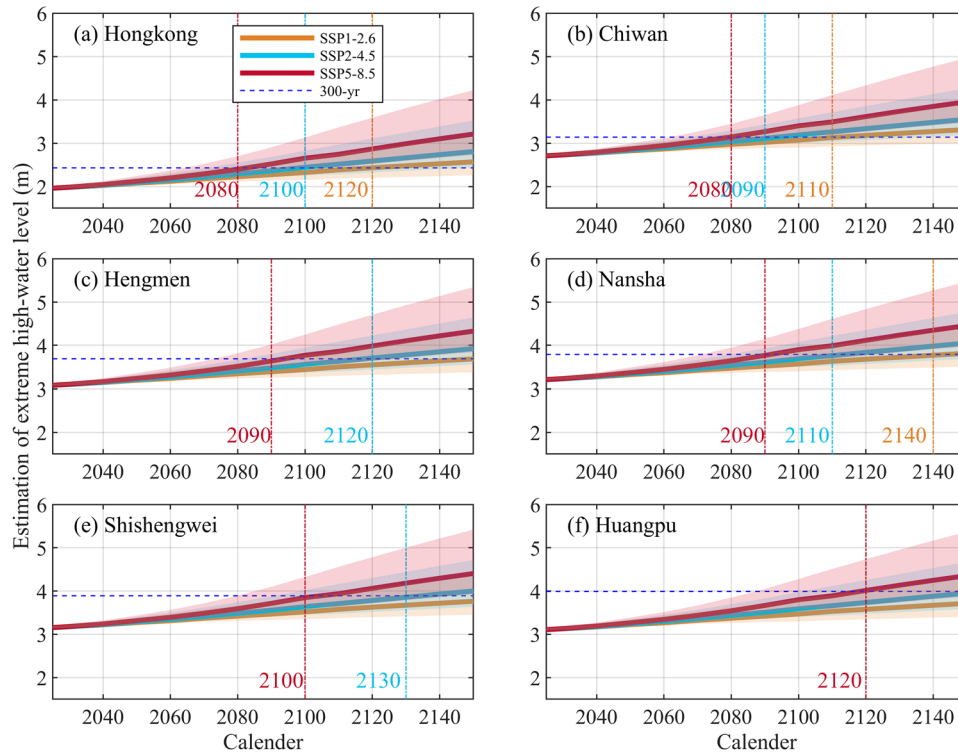


**Figure 10.** Estimation of extreme high water level under IPCC sea level rise scenarios: SSP1-2.6 (low), SSP2-4.5 (intermediate), and SSP5-8.5 (very high).

Lingding Bay confronts the highest imminent flood risk under SLR, while the upper tidal reach maintains relative security.

Based on upon morphodynamic evolution, storm surge classification, risk distribution analysis and the projected future flood risk, priority adaptive strategies for BIC in the Greater Bay Area are hierarchically structured as follows. First, the outer LDB exhibits moderate storm intensity (95th percentile) with declining extreme water levels, enabling Hong Kong to maintain existing defenses while dictating Zhuhai-Macao to upgrade western LDB seawalls to accommodate 2.44 m optimized extreme high water levels for 300-yr return period. Conversely, the inner LDB confronts severe risk, mandating elevated seawall standards (Chiwan: 3.14 m; Hengmen: 3.69 m; Nansha: 3.79 m) and implementing integrated flood-surge management. The SZY region demonstrates heightened vulnerability with frequent strong storms and rising extremes, necessitating substantial optimized extreme high-water level upgrades (Shishengwei: 3.88 m; Huangpu: 3.99 m) to counter funnelling effects and upstream flood risk.

Systematic flood risk evaluations have identified critical infrastructure gaps, compelling immediate government intervention. Comprehensive vulnerability assessments must be conducted to evaluate existing seawall capacity against surge-induced water level increases,

followed by prioritized reinforcement and reconstruction initiatives to achieve 2035 Greater Bay Area resilience standards (300-yr return period). Strategic focus should target high-risk zones (western LDB and SZY), where optimized  $h_{ps}$  predictions surpass original design benchmarks by 0.33-0.47 m, a discrepancy attributable to intensifying tidal dynamics and extreme weather patterns. These measures are essential for safeguarding the region against escalating hydrodynamic threats while meeting evolving water security requirements.

## 5. Conclusions

Frequent estuarine engineering represents critical determinants of flood risk, whereas our understanding of their impact on extreme high water levels remain limited. In this study, we employed an integrated approach combining GEV and max-stable models to systematically assess flood risk variations in the Bay-Inlet-Channel system of the Greater Bay Area. Hydrodynamic analysis elucidated the spatially heterogeneous trends in extreme high water levels, whereas numerical modelling quantified the specific contributions of channel dredging and land reclamation. The principal findings reveal:

- (1) Morphological changes induced by estuarine engineering, particularly channel dredging and land

reclamation, have significantly elevated extreme high water levels and intensified storm severity across the Greater Bay Area.

- (2) Depositional processes attenuating tidal range have moderated flood risk acceleration at the bay mouth (0.22 cm/yr), whereas channel deepening and narrowing resulting from intensive dredging and reclamation have driven more rapid increases in the inner bay (0.65 cm/yr), and the upper tidal reach exhibiting intermediate trends (0.56 cm/yr) due to energy dissipation through Humen Inlet.
- (3) Optimized extreme high water level projections establish scientific foundations for levee design and facilitate estimation of temporal thresholds when water levels exceed 300-yr return levels under three sea-level rise scenarios.

This study addresses a crucial knowledge gap concerning how channel dredging and land reclamation amplify flood risk in mega-bay systems, providing scientific guidance for future flood risk management in the densely populated Greater Bay Area. However, the mechanisms governing compound water level variations (incorporating tides, runoff, and other factors) under anthropogenically modified morphological changes require further investigation. Future research should extend to encompass the complex Pearl River Estuary network to develop a more comprehensive understanding of these hydrodynamic interactions.

### Data access statement

Data openly available in a public repository that issues datasets with DOIs: 10.17632/c2fkypbpf.1.

### Acknowledgements

We would also like to extend sincere gratitude to the following individuals for their invaluable assistance during the data collection: Hao Yang, Bozhi Wang, Huimin Pan, and Bo Li. More details can be obtained from the corresponding author (zjdai@sklec.ecnu.edu.cn; linjliang7@mail.sysu.edu.cn) upon reasonable request.

### Author contributions

CRediT: **Ping Zhang**: Investigation, Methodology, Validation, Visualization, Writing – original draft, Writing – review & editing; **Haichen Liu**: Investigation, Visualization; **Huayang Cai**: Data curation, Resources, Validation; **Suying Ou**: Investigation, Methodology, Validation; **Zhijun Dai**: Conceptualization, Funding acquisition, Investigation, Resources, Supervision, Writing – original draft, Writing – review & editing; **Jianliang Lin**: Conceptualization, Funding acquisition, Software, Visualization, Writing – original draft; **Qingshu Yang**:

Data curation, Funding acquisition, Methodology, Resources, Supervision

### Disclosure statement

No potential conflict of interest was reported by the author(s).

### Funding

This research was supported by the National Natural Science Key Foundation of China (NSFC) (42430406), the National Key R&D of China (2016YFC0402600), National Natural Science Foundation of China (NSFC) (42406159). More details can be obtained from the corresponding author (zjdai@sklec.ecnu.edu.cn; linjliang7@mail.sysu.edu.cn) upon reasonable request.

### References

- Arns, A., Wahl, T., Wolff, C., Vafeidis, A. T., Haigh, I. D., Woodworth, P., Niehüser, S., & Jensen, J. (2020). Non-linear interaction modulates global extreme sea levels, coastal flood exposure, and impacts. *Nature Communications*, 11(1), 1918. <https://doi.org/10.1038/s41467-020-15752-5>
- Boumis, G., Moftakhari, H. R., & Moradkhani, H. (2023). Storm surge hazard estimation along the US gulf coast: A Bayesian hierarchical approach. *Coastal Engineering*, 185, 104371. <https://doi.org/10.1016/j.coastaleng.2023.104371>
- Cai, H., Yang, H., Liu, J., Niu, L., Ren, L., Liu, F., Ou, S., & Yang, Q. (2019). Quantifying the impacts of human interventions on relative mean sea level change in the pearl river delta, China. *Ocean & Coastal Management*, 173, 52–64. <https://doi.org/10.1016/j.ocecoaman.2019.02.007>
- Calafat, F. M., Wahl, T., Tadesse, M. G., & Sparrow, S. N. (2022). Trends in Europe storm surge extremes match the rate of sea-level rise. *Nature*, 603(7903), 841–845. <https://doi.org/10.1038/s41586-022-04426-5>
- Caldwell, P. C., Merrifield, M. A., & Thompson, P. R. (2015). *Sea level measured by tide gauges from global oceans - the Joint Archive for Sea Level holdings (NCEI Accession 0019568), Version 5.5*, NOAA National Centers for Environmental Information [Data set]. <https://doi.org/10.7289/V5V40S7W>
- Candela, J., Winant, C. D., & Bryden, H. L. (1989). Meteorologically forced subinertial flows through the strait of Gibraltar. *Journal of Geophysical Research: Oceans*, 94(C9), 12667–12679. <https://doi.org/10.1029/JC094iC09p12667>
- Cao, Y., & Li, B. (2019). Assessing models for estimation and methods for uncertainty quantification for spatial return levels. *Environmetrics*, 30(2), e2508. <https://doi.org/10.1002/env.2508>
- Chan, F. K. S., Paszkowski, A., Wang, Z., Lu, X., Mitchell, G., Tran, D. D., Warner, J., Li, J., Chen, Y. D., Li, N., Pal, I., Griffiths, J., Chen, J., Chen, W. Q., & Zhu, Y. G. (2024). Building resilience in Asian mega-deltas. *Nature Reviews Earth & Environment*, 5(7), 522–537. <https://doi.org/10.1038/s43017-024-00561-x>
- Chu, N., Yao, P., Ou, S., Wang, H., Yang, H., & Yang, Q. (2022). Response of tidal dynamics to successive land reclamation in the lingding bay over the last century. *Coastal Engineering*, 173, 104095. <https://doi.org/10.1016/j.coastaleng.2022.104095>



- Dai, Z., Fagherazzi, S., Mei, X., Chen, J., & Meng, Y. (2016). Linking the infilling of the north branch in the changjiang (Yangtze) estuary to anthropogenic activities from 1958 to 2013. *Marine Geology*, 379, 1–12. <https://doi.org/10.1016/j.margeo.2016.05.006>
- De Dominicis, M., Wolf, J., van Hespén, R., Zheng, P., & Hu, Z. (2023). Mangrove forests can be an effective coastal defence in the pearl river delta, China. *Communications Earth & Environment*, 4(1), 1–13. <https://doi.org/10.1038/s43247-022-00672-7>
- Doodson, A. T. (1956). Tides and storm surges in a long uniform gulf. *Proceedings of the Royal Society of London. Series in Mathematical and Physical Sciences*, 237(1210), 325–343. <https://doi.org/10.1098/rspa.1956.0180>
- Edmonds, D. A., Caldwell, R. L., Brondizio, E. S., & Siani, S. M. O. (2020). Coastal flooding will disproportionately impact people on river deltas. *Nature Communications*, 11(1), 4741. <https://doi.org/10.1038/s41467-020-18531-4>
- Enríquez, A. R., Wahl, T., Marcos, M., & Haigh, I. D. (2020). Spatial footprints of storm surges along the global coastlines. *Journal of Geophysical Research: Oceans*, 125(9), e2020JC016367. <https://doi.org/10.1029/2020JC016367>
- Familkhali, R., & Talke, S. A. (2016). The effect of channel deepening on tides and storm surge: A case study of wilmington, NC. *Geophysical Research Letters*, 43(17), 9138–9147. <https://doi.org/10.1002/2016GL069494>
- Fisher, R. A., & Tippett, L. H. C. (1928). Limiting forms of the frequency distribution of the largest or smallest member of a sample. *Mathematical Proceedings of the Cambridge Philosophical Society*, 24(2), 180–190. <https://doi.org/10.1017/S0305004100015681>
- Fu, L., Zhong, Y., Zhang, P., Niu, L., Zhang, X., Lin, J., Cai, H., & Yang, Q. (2025). The evolution and morphodynamic characteristics of shoals and troughs in lingdingyang bay of the pearl river estuary. *Frontiers in Marine Science*, 12, 1525805. <https://doi.org/10.3389/fmars.2025.1525805>
- Godin, G. (1972). *The analysis of tides*. Toronto: University of Toronto Press.
- Guo, L., Zhu, C., Xu, F., Xie, W., van der Wegen, M., Townend, I., Wang, Z. B., & He, Q. (2022). Reclamation of tidal flats within tidal basins alters centennial morphodynamic adaptation to sea-level rise. *Journal of Geophysical Research: Earth Surface*, 127(6), e2021JF006556. <https://doi.org/10.1029/2021JF006556>
- Hague, B. S., & Talke, S. A. (2024). The influence of future changes in tidal range, storm surge, and mean Sea level on the emergence of chronic flooding. *Earth's Future*, 12(2), e2023EF003993. <https://doi.org/10.1029/2023EF003993>
- Haigh, I. D., Wadey, M. P., Wahl, T., Ozsoy, O., Nicholls, R. J., Brown, J. M., Horsburgh, K., & Gouldby, B. (2016). Spatial and temporal analysis of extreme sea level and storm surge events around the coastline of the UK. *Scientific Data*, 3(1), 160107. <https://doi.org/10.1038/sdata.2016.107>
- Hoitink, A. J. F., Nittrouer, J. A., Passalacqua, P., Shaw, J. B., Langendoen, E. J., Huismans, Y., & van Maren, D. S. (2020). Resilience of river deltas in the anthropocene. *Journal of Geophysical Research: Earth Surface*, 125(3), e2019JF005201. <https://doi.org/10.1029/2019JF005201>
- Hoshino, S., Esteban, M., Mikami, T., Takagi, H., & Shibayama, T. (2016). Estimation of increase in storm surge damage due to climate change and sea level rise in the greater Tokyo area. *Natural Hazards*, 80(1), 539–565. <https://doi.org/10.1007/s11069-015-1983-4>
- Hu, K., Ding, P., & Ge, J. (2007). *Modeling of storm surge in the coastal waters of Yangtze estuary and Bay*.
- Hu, S., Liu, B., Hu, M., Yu, X., Deng, Z., Zeng, H., Zhang, M., & Li, D. (2023). Quantification of the nonlinear interaction among the tide, surge and river in pearl river estuary. *Estuarine, Coastal and Shelf Science*, 290, 108415. <https://doi.org/10.1016/j.ecss.2023.108415>
- Idier, D., Bertin, X., Thompson, P., & Pickering, M. D. (2019). Interactions between mean Sea level, tide, surge, waves and flooding: Mechanisms and contributions to Sea level variations at the coast. *Surveys in Geophysics*, 40(6), 1603–1630. <https://doi.org/10.1007/s10712-019-09549-5>
- Intergovernmental Panel on Climate Change (IPCC). (2023). Climate change 2022 – impacts, adaptation and vulnerability: Working group II contribution to the sixth assessment report of the intergovernmental panel on climate change. Cambridge University Press, Cambridge.
- Jay, D. A. (1991). Green's law revisited: Tidal long-wave propagation in channels with strong topography. *Journal of Geophysical Research: Oceans*, 96(C11), 20585–20598. <https://doi.org/10.1029/91JC01633>
- Klotzbach, P. J., Wood, K. M., Schreck, C. J., Bowen, S. G., Patricola, C. M., & Bell, M. M. (2025). Trends in Global Tropical Cyclone Activity: 1990–2021. *Geophysical Research Letters*, 49, e2021GL095774. <https://doi.org/10.1029/2021GL095774>
- Lin, N., Marsooli, R., & Colle, B. A. (2019). Storm surge return levels induced by mid-to-late-twenty-first-century extratropical cyclones in the northeastern United States. *Climatic Change*, 154(1–2), 143–158. <https://doi.org/10.1007/s10584-019-02431-8>
- Liu, F., Yuan, L., Yang, Q., Ou, S., Xie, L., & Cui, X. (2014). Hydrological responses to the combined influence of diverse human activities in the pearl river delta, China. *Catena*, 113, 41–55. <https://doi.org/10.1016/j.catena.2013.09.003>
- Lowe, S. A., Cercione, C., McKeon, B., & Corrao, J. (2024). Erosion, flooding, and storm surge on the south shore of staten island, New York city. *Journal of Coastal Research*, 41(2), 235–246. <https://doi.org/10.2112/JCOASTRES-D-24-00021.1>
- Ma, Y., Wu, Y., Shao, Z., Cao, T., & Liang, B. (2022). Impacts of sea level rise and typhoon intensity on storm surges and waves around the coastal area of qingdao. *Ocean Engineering*, 249, 110953. <https://doi.org/10.1016/j.oceaneng.2022.110953>
- Mehrotra, R., & Sharma, A. (2019). A resampling approach for correcting systematic spatiotemporal biases for multiple variables in a changing climate. *Water Resources Research*, 55(1), 754–770. <https://doi.org/10.1029/2018WR023270>
- Meiler, S., Vogt, T., Bloemendaal, N., Ciullo, A., Lee, C.-Y., Camargo, S. J., Emanuel, K., & Bresch, D. N. (2022). Inter-comparison of regional loss estimates from global synthetic tropical cyclone models. *Nature Communications*, 13(1), 6156. <https://doi.org/10.1038/s41467-022-33918-1>
- Moftakhari, H. R., Salvadori, G., AghaKouchak, A., Sanders, B. F., & Matthew, R. A. (2017). Compounding effects of sea level rise and fluvial flooding. *Proceedings of the National Academy of Sciences*, 114(37), 9785–9790. <https://doi.org/10.1073/pnas.1620325114>
- Mondal, I., Jose, F., & Roy, S. K. (2024). Assessment of storm surge and habitat loss during recent hurricanes and its prediction: A case study from southwest Florida using ML-based hydrodynamic models. *Regional Studies in Marine Science*, 77(2024), 103683. <https://doi.org/10.1016/j.rsma.2024.103683>

- Munoz, S. E., Giosan, L., Therrell, M. D., Remo, J. W. F., Shen, Z., Sullivan, R. M., Wiman, C., O'Donnell, M., & Donnelly, J. P. (2018). Climatic control of Mississippi river flood hazard amplified by river engineering. *Nature*, 556(7699), 95–98. <https://doi.org/10.1038/nature26145>
- Nanditha, J. S., & Mishra, V. (2025). Multiday precipitation is a prominent driver of floods in Indian river basins.
- Palmer, K., Watson, C., & Fischer, A. (2019). Non-linear interactions between sea-level rise, tides, and geomorphic change in the Tamar Estuary, Australia. *Estuarine, Coastal and Shelf Science*, 225, 106247. <https://doi.org/10.1016/j.ecss.2019.106247>
- Pan, Y. (2024). Analysis of design tide level of Guangzhou reach and Badakou gate in Pearl river delta. *Water Resources Planning and Design*, 06, 26–32. <https://doi.org/10.3969/j.issn.1672-2469.2024.06.006>. In Chinese.
- Piecuch, C. G., Coats, S., Dangendorf, S., Landerer, F. W., Reager, J. T., Thompson, P. R., & Wahl, T. (2022). High-tide floods and storm surges during atmospheric rivers on the US west coast. *Geophysical Research Letters*, 49(2), e2021GL096820. <https://doi.org/10.1029/2021GL096820>
- Rashid, M. M., Moftakhari, H., & Moradkhani, H. (2024). Stochastic simulation of storm surge extremes along the contiguous United States coastlines using the max-stable process. *Communications Earth & Environment*, 5(1), 1–10. <https://doi.org/10.1038/s43247-024-01206-z>
- Rego, J. L., & Li, C. (2010). Nonlinear terms in storm surge predictions: Effect of tide and shelf geometry with case study from Hurricane Rita. *Journal of Geophysical Research Oceans*, 115(C6), C06020. <https://doi.org/10.1029/2009JC005285>
- Rentschler, J., Avner, P., Marconcini, M., Su, R., Strano, E., Voudoukas, M., & Hallegatte, S. (2023). Global evidence of rapid urban growth in flood zones since 1985. *Nature*, 622(7981), 87–92. <https://doi.org/10.1038/s41586-023-06468-9>
- Rentschler, J., Salhab, M., & Jafino, B. A. (2022). Flood exposure and poverty in 188 countries. *Nature Communications*, 13(1), 3527. <https://doi.org/10.1038/s41467-022-30727-4>
- Russo, T. A., Fisher, A. T., & Winslow, D. M. (2013). Regional and local increases in storm intensity in the San Francisco bay area, USA, between 1890 and 2010. *Journal of Geophysical Research: Atmospheres*, 118(8), 3392–3401. <https://doi.org/10.1002/jgrd.50225>
- Savenije, H. H. G., Toffolon, M., Haas, J., & Veling, E. J. M. (2008). Analytical description of tidal dynamics in convergent estuaries. *Journal of Geophysical Research Oceans*, 113(C10), C10025. <https://doi.org/10.1029/2007JC004408>
- Scheuerer, M., Hamill, T. M., Whitin, B., He, M., & Henkel, A. (2017). A method for preferential selection of dates in the schaafe shuffle approach to constructing spatiotemporal forecast fields of temperature and precipitation. *Water Resources Research*, 53(4), 3029–3046. <https://doi.org/10.1029/2016WR020133>
- Schrijvershof, R. A., van Maren, D. S., Van der Wegen, M., & Houtink, A. J. F. (2024). Land reclamation controls on multi-centennial estuarine evolution. *Earth's Future*, 12(11), e2024EF005080. <https://doi.org/10.1029/2024EF005080>
- She, Z., Huang, L., Cai, H., Fan, M., Yu, L., Li, B., Lan, X., Chen, X., & Liu, Z. (2023). Detecting human interventions by spatial dependence of extreme water levels using a high dimensional conditional probability approach over the pearl river delta. *Journal of Hydrology*, 622, 129681. <https://doi.org/10.1016/j.jhydrol.2023.129681>
- Stephens, S. A., Bell, R. G., & Haigh, I. D. (2020). Spatial and temporal analysis of extreme storm-tide and skew-surge events around the coastline of New Zealand. *Natural Hazards and Earth System Sciences*, 20(3), 783–796. <https://doi.org/10.5194/nhess-20-783-2020>
- Stoev, S. A. (2010). Max-stable processes: Representations, ergodic properties and statistical applications. In P. Doukhan, G. Lang, D. Surgailis, & G. Teyssi re (Eds.), *Dependence in probability and statistics* (pp. 21–42). Springer.
- Tadesse, M. G., Wahl, T., Rashid, M. M., Dangendorf, S., Rodr guez-Enr quez, A., & Talke, S. A. (2022). Long-term trends in storm surge climate derived from an ensemble of global surge reconstructions. *Scientific Reports*, 12(1), 13307. <https://doi.org/10.1038/s41598-022-17099-x>
- Talke, S. A., Orton, P., & Jay, D. A. (2014). Increasing storm tides in New York harbor, 1844–2013. *Geophysical Research Letters*, 41(9), 3149–3155. <https://doi.org/10.1002/2014GL059574>
- Van Maren, D. S., Beemster, J. G. W., Wang, Z. B., Khan, Z. H., Schrijvershof, R. A., & Houtink, A. J. F. (2023). Tidal amplification and river capture in response to land reclamation in the Ganges-Brahmaputra delta. *CATENA*, 220, 106651. <https://doi.org/10.1016/j.catena.2022.106651>
- Voudoukas, M. I., Mentaschi, L., Voukouvalas, E., Verlaan, M., Jevrejeva, S., Jackson, L. P., & Feyen, L. (2018). Global probabilistic projections of extreme sea levels show intensification of coastal flood hazard. *Nature Communications*, 9(1), 2360. <https://doi.org/10.1038/s41467-018-04692-w>
- Wahl, T., Haigh, I. D., Nicholls, R. J., Arns, A., Dangendorf, S., Hinkel, J., & Slangen, A. B. A. (2017). Understanding extreme sea levels for broad-scale coastal impact and adaptation analysis. *Nature Communications*, 8(1), 16075. <https://doi.org/10.1038/ncomms16075>
- Wahl, T., Jain, S., Bender, J., Meyers, S. D., & Luther, M. E. (2015). Increasing risk of compound flooding from storm surge and rainfall for major US cities. *Nature Climate Change*, 5(12), 1093–1097. <https://doi.org/10.1038/nclimate2736>
- Walters, R., & Heston, C. (1982). Removing tidal-period variations from time-series data using low-pass digital filters. *Journal of Physical Oceanography*, 12(1), 112–115. [https://doi.org/10.1175/1520-0485\(1982\)012<0112:RTPVFT>2.0.CO;2](https://doi.org/10.1175/1520-0485(1982)012<0112:RTPVFT>2.0.CO;2)
- Wang, X., Guo, Y., & Ren, J. (2021). The coupling effect of flood discharge and storm surge on extreme flood stages: A case study in the pearl river delta, south China. *International Journal of Disaster Risk Science*, 12(4), 1–15. <https://doi.org/10.1007/s13753-021-00355-5>
- Wang, W.-X., & Rainbow, P. S. (2020). *Environmental pollution of the pearl river estuary, China: Status and impact of contaminants in a rapidly developing region, estuaries of the world*. Springer.
- Wang, Z. B., Van Maren, D. S., Ding, P. X., Yang, S. L., Van Prooijen, B. C., De Vet, P. L. M., Winterwerp, J. C., De Vriend, H. J., Stive, M. J. F., & He, Q. (2015). Human impacts on morphodynamic thresholds in estuarine systems. *Continental Shelf Research, Coastal Seas in a Changing World: Anthropogenic Impact and Environmental Responses*, 111(Part B), 174–183. <https://doi.org/10.1016/j.csr.2015.08.009>

- Wei, X., Cai, S., & Zhan, W. (2021). Impact of anthropogenic activities on morphological and deposition flux changes in the Pearl River Estuary, China. *Scientific Reports*, 11(1), 16643. <https://doi.org/10.1038/s41598-021-96183-0>
- Wu, Z., Milliman, J. D., Zhao, D., Cao, Z., Zhou, J., & Zhou, C. (2018). Geomorphologic changes in the lower pearl river delta, 1850-2015, largely due to human activity. *Geomorphology*, 314, 42–54. <https://doi.org/10.1016/j.geomorph.2018.05.001>
- Wu, C., Ren, J., Bao, Y., Shi, H., & Tang, Z. (2006). A preliminary study on the morphodynamic evolution of the “gate” of the pearl river delta, China. *Acta Geologica Sinica*, 61(5), 537–548. <https://doi.org/10.11821/xb200605010>
- Wu, Z. Y., Saito, Y., Zhao, D. N., Zhou, J. Q., Cao, Z. Y., Li, S. J., Shang, J. H., & Liang, Y. Y. (2016). Impact of human activities on subaqueous topographic change in lingding bay of the pearl river estuary, People's Republic of China, during 1955–2013. *Scientific Reports*, 6(1), 37742. <https://doi.org/10.1038/srep37742>
- Wu, C., Xing, W., Jie, R., Yun, B., Zhigang, H., Yiaping, L., Heyin, S., & Wenyan, Z. (2010). Morphodynamics of the rock-bound outlets of the pearl river estuary, south China — A preliminary study. *Journal of Marine Systems*, Pearl River Estuary related sediments as response to Holocene climate change and anthropogenic impact (PECAI), 82, S17–S27. <https://doi.org/10.1016/j.jmarsys.2010.02.002>
- Yang, J., Yan, F., & Chen, M. (2021). Effects of sea level rise on storm surges in the south yellow Sea: A case study of Typhoon Muifa (2011). *Continental Shelf Research*, 215, 104346. <https://doi.org/10.1016/j.csr.2021.104346>
- You, J., Wang, S., & Zhang, B. (2024). Spatially seamless and temporally continuous assessment on compound flood risk in Hong Kong. *Journal of Hydrology*, 645, 132217. <https://doi.org/10.1016/j.jhydrol.2024.132217>
- Zhang, W., Cao, Y., Zhu, Y., Zheng, J., Ji, X., Xu, Y., Wu, Y., & Hoitink, A. J. F. (2018). Unravelling the causes of tidal asymmetry in deltas. *Journal of Hydrology*, 564, 588–604. <https://doi.org/10.1016/j.jhydrol.2018.07.023>
- Zhang, M., Dai, Z., Bouma, T. J., Bricker, J., Townend, I., Wen, J., Zhao, T., & Cai, H. (2021a). Tidal-flat reclamation aggravates potential risk from storm impacts. *Coastal Engineering*, 166, 103868. <https://doi.org/10.1016/j.coastaleng.2021.103868>
- Zhang, W., Feng, H., Zheng, J., Hoitink, A. J. F., van der Vegt, M., Zhu, Y., & Cai, H. (2013). Numerical simulation and analysis of saltwater intrusion lengths in the pearl river delta, China. *Journal of Coastal Research*, 29(2), 372–382. <https://doi.org/10.2112/JCOASTRES-D-12-00068.1>
- Zhang, P., Yang, Q., Wang, H., Cai, H., & Jia, L. (2021b). Stepwise alterations in tidal hydrodynamics in a highly human-modified estuary: The roles of channel deepening and narrowing. *Journal of Hydrology*, 597, 126153. <https://doi.org/10.1016/j.jhydrol.2021.126153>
- Zhou, Y., Shan, Y., Liu, G., & Guan, D. (2018). Emissions and low-carbon development in guangdong-Hong Kong-macao greater bay area cities and their surroundings. *Applied Energy*, 228, 1683–1692. <https://doi.org/10.1016/j.apenergy.2018.07.038>
- Zhu, C., van Maren, D. S., Guo, L., Xie, W., Xing, C., Wang, Z. B., & He, Q. (2025). Water and sediment exchange between the anthropogenically modified distributaries of the Yangtze estuary. *CATENA*, 250, 108729. <https://doi.org/10.1016/j.catena.2025.108729>
- Zhuge, W., Wu, G., Liang, B., Yuan, Z., Zheng, P., Wang, J., & Shi, L. (2024). A statistical method to quantify the tide-surge interaction effects with application in probabilistic prediction of extreme storm tides along the northern coasts of the South China Sea. *Ocean Engineering*, 298, 117151. <https://doi.org/10.1016/j.oceaneng.2024.117151>